Proceedings of ASME Turbo Expo 2023
Turbomachinery Technical Conference and Exposition
GT2023
June 26-30, 2023, Boston, Massachusetts

GT2023-104204

THE IMPACT OF OXIDATION-INDUCED DEGRADATION ON MATERIALS USED IN HYDROGEN-FIRED MICROTURBINES

Marie Romedenne
Materials Science and Technology Division, Oak Ridge National Laboratory, Oak Ridge, TN

Rishi Pillai
Materials Science and Technology Division, Oak Ridge National Laboratory, Oak Ridge, TN

Sebastien Dryepondt
Materials Science and Technology Division, Oak Ridge National Laboratory, Oak Ridge, TN

Bruce Pint
Materials Science and Technology Division, Oak Ridge National Laboratory, Oak Ridge, TN

ABSTRACT

Hydrogen-fueled microturbines are being considered as part of the future green microgrid. However, the use of hydrogen as a fuel presents new challenges for selection and development of suitable high temperature materials for hydrogen combustion. The burning of hydrogen is expected to result in higher operating temperatures and higher than typically observed water vapor contents in exhaust gases versus burning natural gas. In the present work, foil specimens of various Fe- and Ni-based alloys were oxidized in air + 10 % H_2O and air + 60% H_2O for up to 5,000 h at 700 °C to simulate the exhaust atmosphere of natural gas and hydrogen-fueled microturbines. The impact of alloy composition and water vapor content on the oxidation/ volatilization induced loss of wall thickness was experimentally evaluated. Enhanced external oxidation and volatilization of Cr_2O_3 and Ti-doped Cr_2O_3 scales was observed in air + 60% H_2O compared to air + 10% H_2O. No significant impact of the higher water vapor content was observed on Al_2O_3 scales formed on Fe-based alumina forming alloys. Lifetime modeling was employed to predict the combined effects of water vapor content, gas flow rates, temperature and alloy composition on the oxidation-induced lifetime of the investigated materials.

Keywords: Foil oxidation, water vapor, microturbine, lifetime

NOMENCLATURE

wt.%	Composition in weight percent
vol.%	Composition in volume percent
k_p	Oxidation rate constant in $mg^2.cm^{-4}.h^{-1}$
$p^{(i)}$	$CrO_2(OH)_2$ partial pressure (atm) close to the specimen surface
$p^{(0)}$	$CrO_2(OH)_2$ partial pressure (atm) away from the specimen surface
$K_{CrO_2(OH)_2}$	$CrO_2(OH)_2$ equilibrium constant
p_{H_2O}	H_2O partial pressure
p_{O_2}	O_2 partial pressure
D	Binary gas diffusion coefficient
R	Universal gas constant
T	Temperature
v	kinematic viscosity
u	gas velocity
l	specimen length
M_{Cr}	Molar mass of Cr

1. INTRODUCTION

The use of hydrogen as a fuel produced from renewables or traditional sources has been identified as integral to decarbonize the energy, industrial and transportation sectors (1-4). The transition to a hydrogen economy faces, however, many challenges such as reliable and efficient storage and transport (5). Materials lifetime challenges are also associated with the use of hydrogen fueled turbines and microturbines since water vapor will be present in increased amount in the exhaust atmosphere (6-8).

Water vapor in the exhaust atmosphere of natural gas fueled turbines (usually simulated as a mixture of air with 10 vol.% H_2O) was shown to affect lifetime of Ni-based chromia-forming alloys by enhancing the transition from Cr-rich and slow growing oxides to fast growing and non-protective mixed oxides through oxidation and volatilization processes (9-15). Increased Cr_2O_3 growth rates and enhanced adherence were revealed by Zurek *et al.* in Ar-4%H_2-7%H_2O compared to Ar-20% O_2 after two stage oxidation experiments using $^{18}O_2$- and $H_2{}^{18}O$-tracers at 1050 °C (16). Increased mass losses, thicker oxide scales and increased precipitate free zone thicknesses were measured for 0.5 mm thick Hastelloy X (Ni-22Cr-18Fe-9Mo) after 1,000 h in air + 10 % H_2O as compared to dry air at 950 °C (10 h cycles)

suggesting increased growth rates, Cr consumption and decreased adherence in the presence of water vapor (11).

Other parameters such as specimen thickness (11, 17) and alloy composition (13) were also found to affect components lifetimes. Decreased oxidation lifetime (time to depletion to less than 10 wt.% Cr at the oxide/ alloy interface (17, 18), t_{10}) were observed for 0.2 mm alloy 230 (Ni-22Cr-14W) foils compared to thicker 0.3 and 0.5 mm ones during cyclic oxidation between 950 and 1050 °C in air (17). Similarly, lower oxidation lifetimes (t_{10}) were predicted for alloy 120 than alloy 625 (Ni-21Cr-9Mo) between 700 and 800 °C in dry air and air + 10 % H_2O (14), in agreement with experimental observations (13). Very limited literature has shown accelerated degradation and enhanced formation of transient oxides of Ni-based superalloys in simulated exhaust atmosphere of hydrogen-fueled gas turbines (> 20 % H_2O) at 800 and 1,000 °C (7). A better understanding on the long-term oxidation behavior of high temperature alloys in varying water vapor contents is essential to the commercial viability of hydrogen power generation systems.

The aim of the present work is to study the impact of increased water vapor content on the oxidation behavior of candidate foils for hydrogen-fired microturbines. A precipitation-strengthened (γ') chromia-forming Ni-based alloy Haynes® alloy 282 (19), a solid-solution and precipitation-strengthened (Cr-rich carbides) marginal alumina-forming Ni-based alloy 602CA (20) and a precipitation-strengthened (γ', Laves and β-NiAl) alumina-forming austenitic alloy (AFA) were exposed in flowing air + 10 % H_2O and air + 60 % H_2O at 700 °C. The roles of water vapor, alloy composition and foil thickness on the component lifetime were evaluated. A lifetime model was employed to increase understanding and predict the oxidation- and volatilization-induced Cr losses during exposure in flowing air + 10 % H_2O and air + 60 % H_2O.

2. MATERIALS AND METHODS

Rectangular foil specimens (20 mm × 10 mm) of: 1) Haynes® alloy 282 (178 ± 2 µm thick), 2) cold rolled and annealed VDM® alloy 602CA (65 and 200 µm thick) and 3) hot-forged, hot-rolled, cold-rolled and annealed for 1 h at 1,100 °C alumina forming alloy (AFA) (110 µm thick) were placed in alumina boats and exposed in a horizontal alumina tube furnace (internal diameter of 5.9 cm) heated by a three-zone furnace with three independent temperature settings for up to 5,000 h (500 h cycles) in flowing air + 10 vol.% H_2O (henceforth named $10H_2O$) and air + 60 vol.% H_2O (henceforth named $60H_2O$). The gas flow rate was set at 850 $cm^3.min^{-1}$ or 1.7 $cm.s^{-1}$ and the temperature was 700 °C (minimum desired temperature of advanced microturbines (21)). The wall's temperature profile was precisely measured every centimeter along the tube, using a type S thermocouple to allow an isothermal zone of 23 cm with a temperature of 700 ± 4 °C between 51 and 74 cm from the inlet. The volumetric gas flow rates were managed thanks to mechanical gas flow meters and controllers.

A pneumatic pump was used to inject the water through stainless steel capillaries into the flowing gas stream heated above its condensation temperature. All capillaries were heated at around 200 °C using heating tape to avoid water condensation. Water was collected and measured after flowing through the capillaries to calibrate the amount of injected water at 10 ± 1 vol.% H_2O and 60 ± 1 vol.% H_2O which corresponded to 4.5 and 61.5 mL of H_2O consumed per hour respectively. The water was condensed at the end of the alumina tube. The water vapor content and gas flow rates were monitored weekly at the capillary inlet. However, due to an accidental laboratory power outage, the heating was interrupted for 48 h at around 2,900 h in $60H_2O$. In addition, after 3900 h, the stainless-steel capillary broke and had to be replaced. The use of a defective capillary might have resulted in lower water vapor content injected into the furnace between 3,400 and 3,900 h (one 500h cycle). The corresponding time when the capillary failed for other 282 and 602CA specimens, that were added later in the furnace, was 1,500 h. These specimens were removed and replaced after the capillary was changed and exposed for 1,500 h. Mass changes, oxide scales and Cr losses were similar between the two 1,500 h exposures, suggesting a minimal impact of the capillary failure on the oxidation behavior of the 5,000 h specimens. Before exposure, the specimens were used in their bright surface finish. Native oxides were present on the surface of the AFA specimens. The chemical compositions of the studied alloys are given in Table 1.

TABLE 1: CHEMICAL COMPOSITION OF STUDIED ALLOYS DETERMINED BY PLASMA AND COMBUSTION ANALYSES

Wt.%	282	602CA	AFA LZ2
Ni	57.4	62.3	25.1
Cr	19.2	25.2	14.9
Al	1.54	2.25	3.98
Fe	0.21	9.5	51.8
Co	10.75	-	-
Mo	8.56	-	2.01
Ti	2.11	0.15	-
Mn	0.08	0.08	1.93
Si	0.08	0.06	0.15
Nb	-	-	2.44
Y	-	0.08	0.01
Zr	-	0.07	0.09
C	0.06	0.16	0.10
S	Not measured	<0.002	10 wppm

Specimens mass changes were measured after every 500 h cycles using a Mettler-Toledo model XP205 balance with an accuracy of ± 0.04 mg or ± 0.01 $mg.cm^{-2}$. After exposure, specimens were Cu plated and mounted in conductive epoxy for cross-sectional characterization including Scanning Electron Microscopy (SEM), Back-scattered Electron (BSE) microscopy (SEM TESCAN model MIRA3) and energy dispersive X-ray spectroscopy (EDS) (EDAX Octane Elect Super Silicon Drift Detector).

3. RESULTS

3.1 Mass change data

Figure 1 shows the measured mass change as a function of time for alloys 282, 602CA (65 and 200 µm thick) in 10H_2O for up to 3,500 h (Figure 1a) and alloys 282, 602CA (65 and 200 µm thick) and AFA in 60H_2O for up to 5,000 h at 700 °C (Figure 1b).

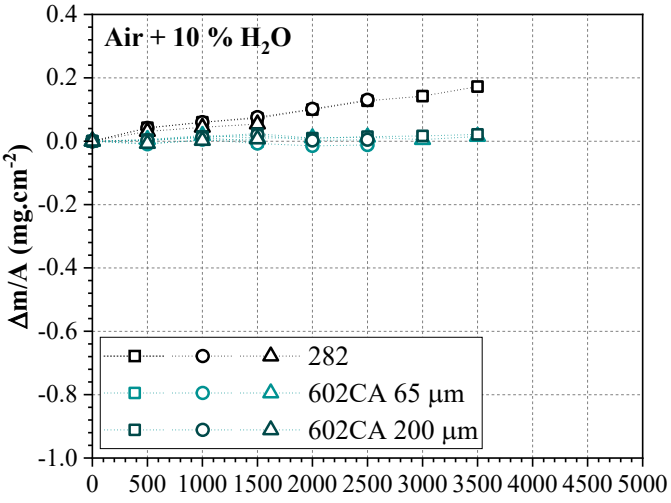

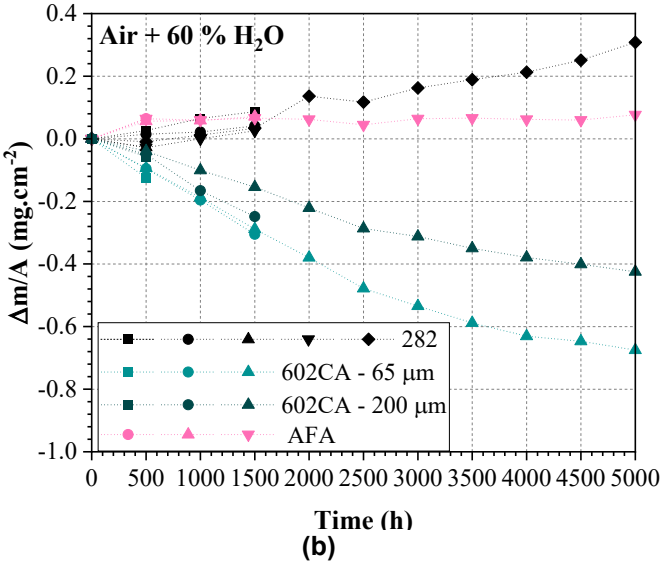

FIGURE 1: MEASURED MASS AS A FUNCTION OF TIME FOR ALLOYS (a) 282 AND 602CA IN FLOWING AIR + 10 % H_2O AND (b) 282, 602CA AND AFA IN FLOWING AIR + 60 % H_2O AT 700 °C.

Similar mass gains were observed for alloy 282 in both environments (Figure 1). For alloy 602CA, low mass gains were measured in 10H_2O (0.02 ± 0.01 mg.cm^{-2} after 3,500 h, Figure 1a) and mass losses were measured in 60H_2O (-0.6 mg.cm^{-2} and -0.3 mg.cm^{-2} after 3,500 h for 65 and 200 µm thick foils after 3,500 h, Figure 1b). Mass losses increased at a slower rate between 3,500 and 5,000 h than between 1,500 and 3,500 h (Figure 1b). Mass losses reached -0.64 and -0.42 for the 65 and 200 µm foils respectively after 5,000 h in 60H_2O (Figure 1b). The AFA alloy was only tested in 60H_2O and demonstrated low mass gains (0.07 mg.cm^{-2} after both 3,500 h and 5,000 h, Figure 1b).

3.2 Oxidation behavior of alloy 282

BSE images and quantified EDS elemental maps of the 282 specimen after 1,500 h in both environments are reported in Figures 2 and 3.

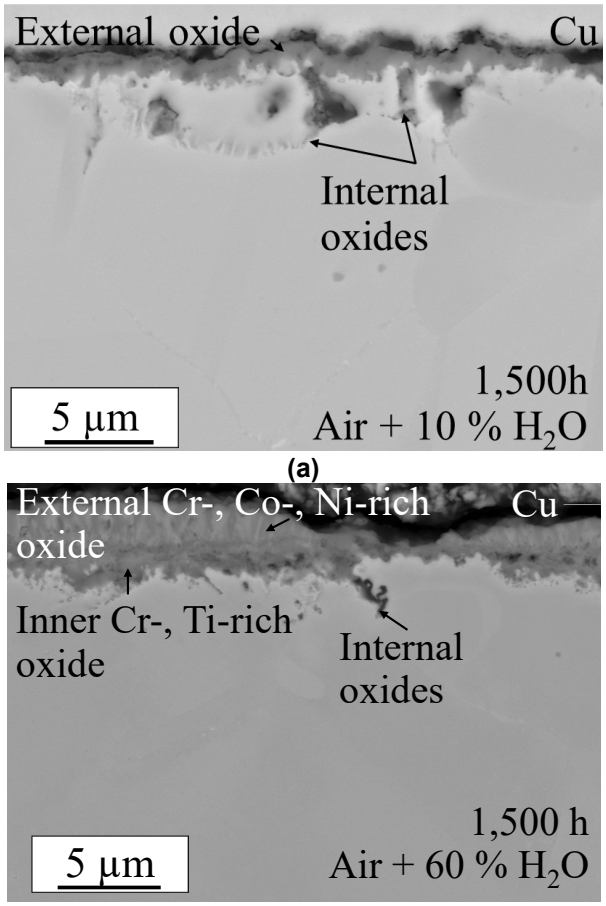

FIGURE 2: BSE IMAGES OF ALLOY 282 AFTER 1,500 H EXPOSURE IN (a) AIR + 10 % H_2O AND (b) AIR + 60 % H_2O AT 700 °C.

Although similar mass gains were measured in both environments (Figure 1), BSE images revealed different oxidation behaviors on alloy 282 after 1,500 h in 10H_2O and 60H_2O. Cr- and Ti-rich external oxide layers (1.58 ± 0.3 µm thick) and Al-rich intergranular oxides were formed after 1,500 h in 10H_2O (Figures 2a and 3a) and Cr-, Co-, Ni-rich, Cr- and Ti-rich external oxide layers (3.7 ± 0.6 µm thick) and Al-, Cr- and Ti- intergranular oxides (3.4 ± 0.4 µm thick) were formed in 60H_2O (Figures 2b and 3b). In addition, Cr-depleted

zones were observed beneath the oxide scale. The depletion depths were not uniform and deep Cr depletion depths were observed along the grain boundaries of the alloy (Figure 3)

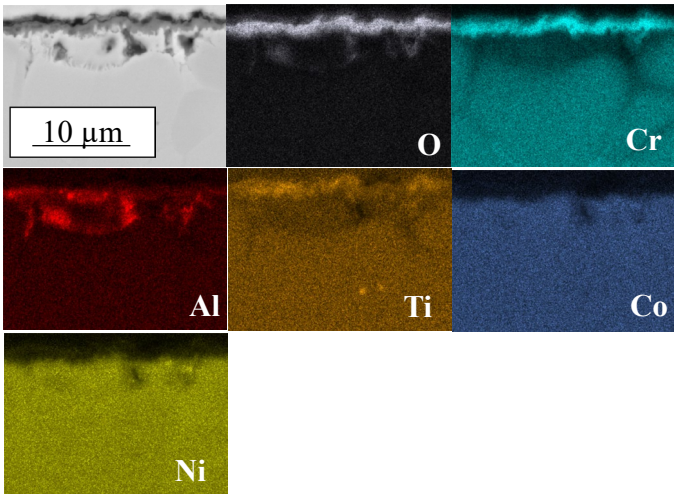

(a)

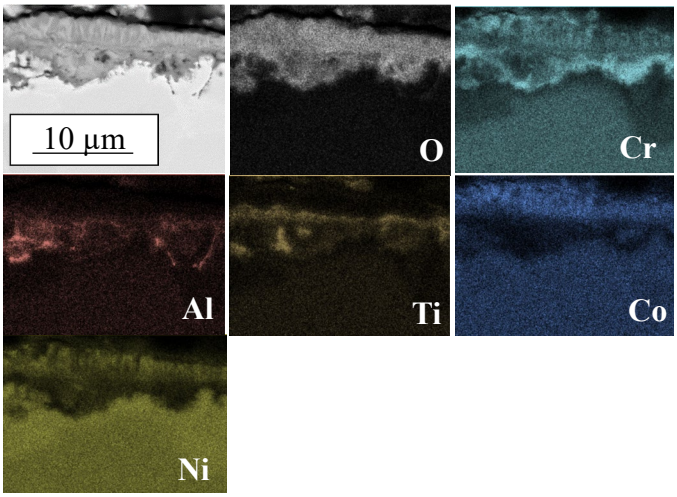

(b)

FIGURE 3: EDS ELEMENTAL MAPS OF ALLOY 282 AFTER 1,500 H EXPOSURE IN (a) AIR + 10 % H_2O AND (b) AIR + 60 % H_2O AT 700 °C.

The inner Cr and Ti-rich oxide scales formed in 60H_2O grew thicker between 1,500 and 5,000 h (from 3.4 ± 0.4 µm to 7.3 ± 1.8 µm, Figures 2b and 4) while the thickness of the outer Cr-, Co- and Ni-rich layer did not vary significantly (Figures 2b and 4). EDS elemental composition profiles measured from the oxide/ alloy interface into the alloy revealed lower Cr and Ti concentrations at the oxide / alloy interface in 60H_2O than in 10H_2O after 1,500 h (Figure 5). Three lines scans were averaged to account for the variability in Cr and Ti depletion depths observed in Figure 3.

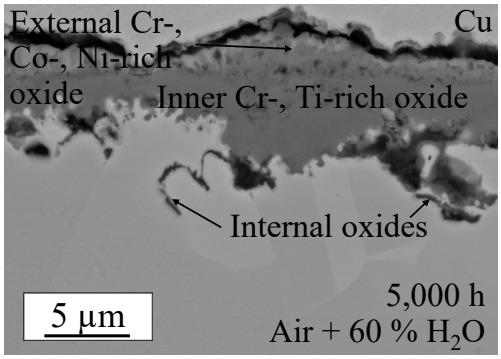

FIGURE 4: BSE IMAGES OF ALLOY 282 AFTER 5,000 H EXPOSURE IN AIR + 60 % H_2O AT 700 °C

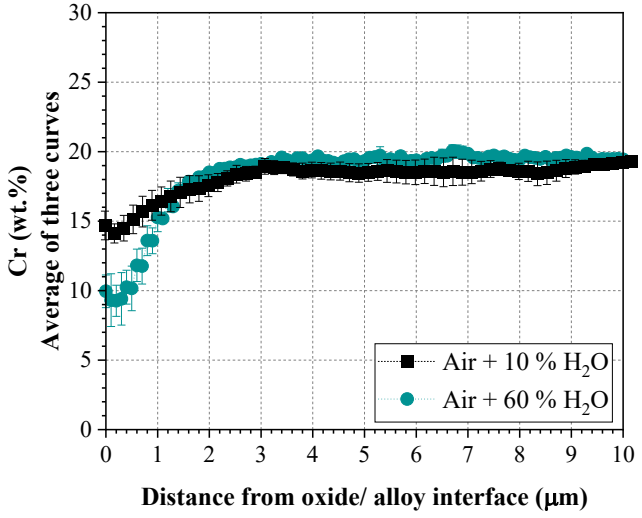

(a)

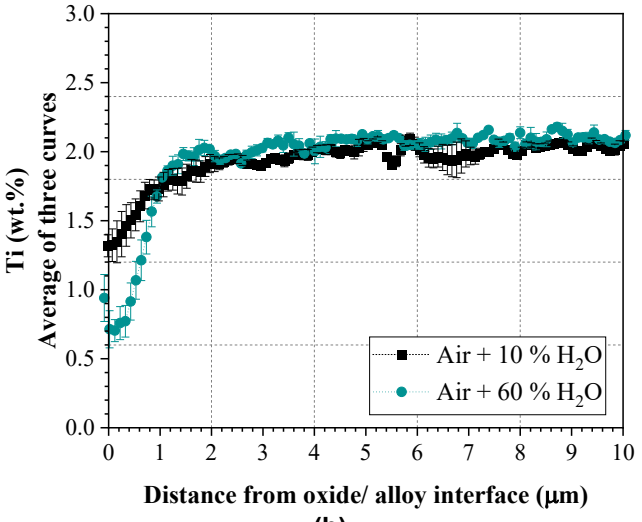

(b)

FIGURE 5: EDS (a) CR and (b) TI ELEMENTAL CONCENTRATION PROFILES WITHIN ALLOY 282 AFTER 1,500 H EXPOSURE IN AIR + 10 % H_2O AIR + 60 % H_2O AT 700 °C. AVERAGE OF THREE LINE SCANS AND RESPECTIVE STANDARD ERRORS ARE REPORTED.

By integrating the Cr and Ti depleted areas and using an alloy density of 8.27 g.cm^{-3}, the amount of Cr and Ti losses (in mg.cm^{-2}) on one side of the foils in each environment were calculated and reported in Table 2. It is clear from Table 2 that 1.5 to 2 times greater Cr and Ti losses were measured after 1,500 h in 60H_2O than in 10H_2O at 700 °C.

TABLE 2: CR AND TI LOSSES DETERMINED BY INTEGRATING DEPLETION PROFILES IN FIGURE 5.

	Air + 10 % H_2O 1,500 h	**Air + 60 % H_2O 1,500 h**
Cr loss (mg.cm^{-2}) – one side	5.5×10^{-2}	8.1×10^{-2}
Ti loss (mg.cm^{-2}) – one side	5×10^{-3}	9×10^{-3}

3.3 Oxidation behavior of alloy 602CA

BSE images and quantified EDS elemental maps of alloy 602CA (65 µm) after 1,500 h in both environments are shown in Figures 6 and 7.

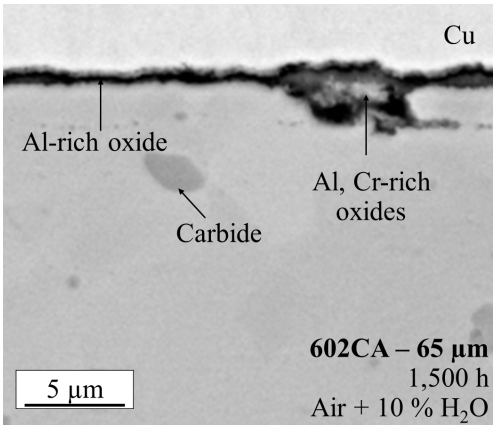

FIGURE 6: BSE OF ALLOY 602CA (65 µm FOIL THICKNESS) AFTER 1,500 H EXPOSURE IN (a) AIR + 10 % H_2O AND (b) AIR + 60 % H_2O AT 700 °C.

In case of the thinner 602CA (65 µm) foil, a mostly thin Al-rich external layer was formed after 1,500 h in 10H_2O (Figures 6a and 7a). Locally Cr-rich external oxides and Al-rich internal oxides were observed. In 60H_2O, an external Cr-rich oxide scale was formed along with the formation of Al- and Cr-rich internal oxides (Figures 6b and 7b).

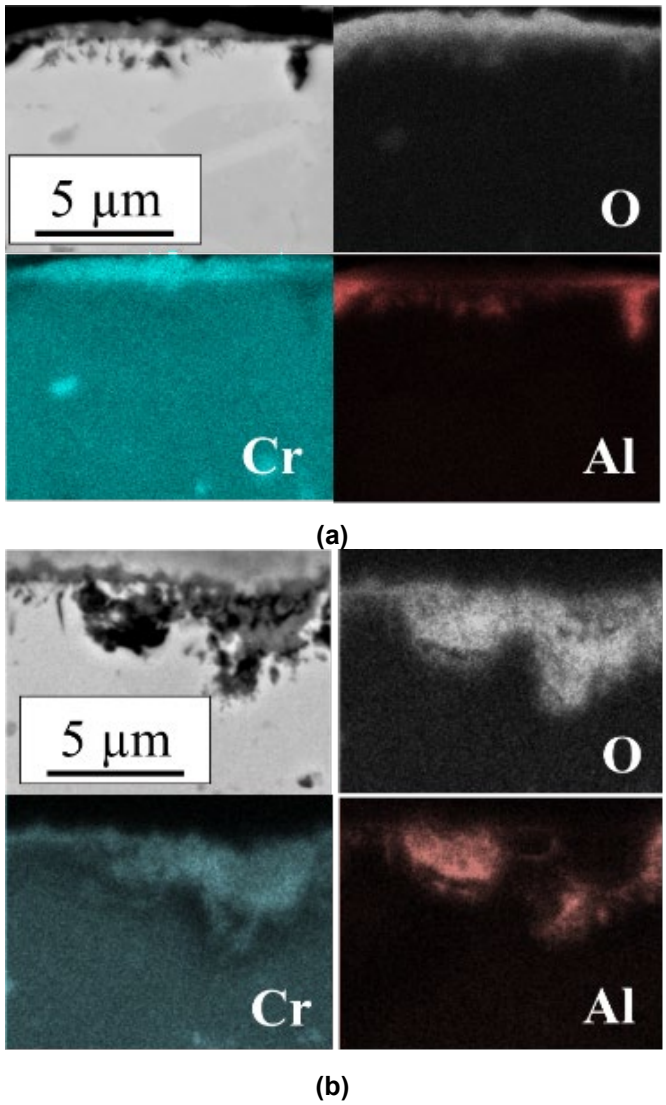

FIGURE 7: EDS ELEMENTAL MAPS OF ALLOY 602CA (65 µm FOIL THICKNESS) AFTER 1,500 H EXPOSURE IN (a) AIR + 10 % H_2O AND (b) AIR + 60 % H_2O AT 700 °C.

EDS elemental composition profiles measured from the alloy/ oxide interface into the alloy did not reveal significant differences between the Cr depletion profiles after 1,500 h in both environments (Figures 8a and 8b). The Cr depletion depths and concentrations at the oxide/ alloy interface did not significantly change between 1,500 and 3,500 h in 10H_2O (Figure 8a). However, after 5,000 h, large Cr depletions depths (7 µm) and low Cr concentration at the alloy/ oxide interface (10 wt.%) were observed in 60H_2O

(Figure 8b). The Cr-rich oxide scale observed after 1,500 h was replaced by thick Fe- and Cr-rich mixed oxides after 5,000 h in 60H_2O suggesting accelerated Cr consumption within the 602CA foil (Figure 9) in agreement with the deep Cr depletion depths measured in Figure 8b.

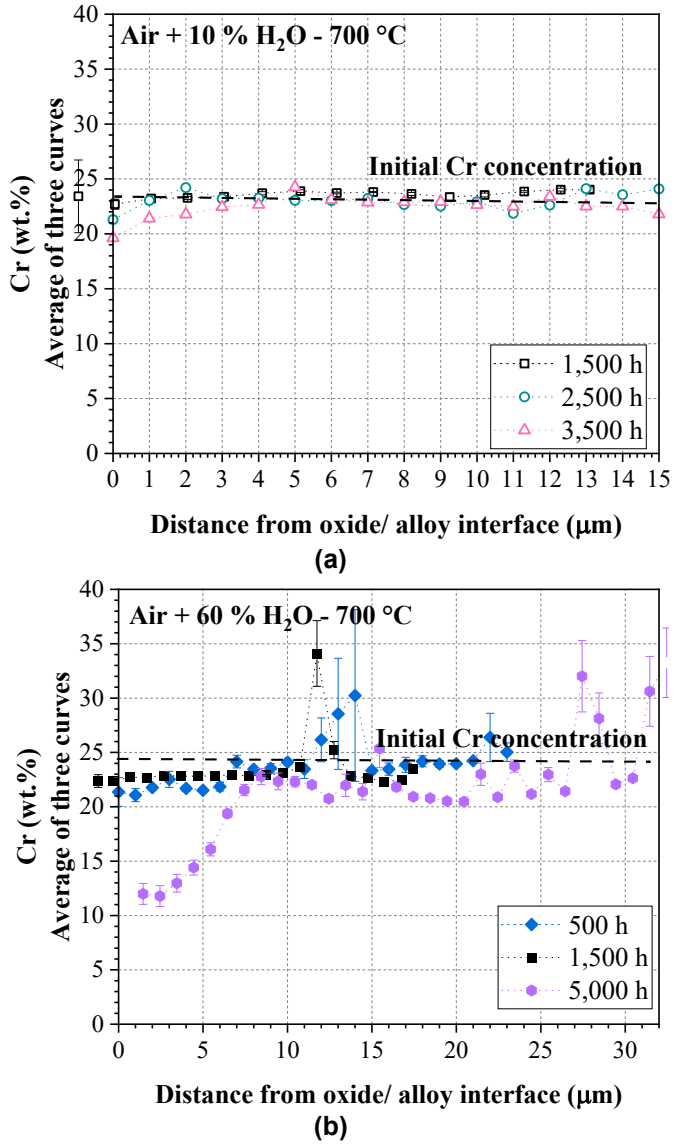

FIGURE 8: EDS CR ELEMENTAL DEPLETION PROFILES WITHIN 602CA (65 µm FOIL THICKNESS) ALLOY AFTER EXPOSURE IN (a) AIR + 10 % H_2O AND (b) AIR + 60 % H_2O AT 700 °C.

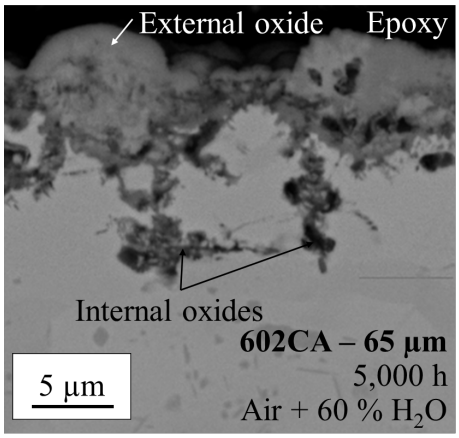

FIGURE 9: BSE IMAGES AND EDS ELEMENTAL MAPS OF ALLOY 602CA (65 µm FOIL THICKNESS) AFTER 5,000 H EXPOSURE IN AIR + 60 % H_2O AT 700 °C.

In addition, deeper Al depletion profiles were observed in 60H_2O than in 10H_2O after 1,500 h (Figure 10) suggesting increased Al consumption in 60H_2O compared to 10H_2O, in agreement with the presence of Al-rich internal oxides below the Cr-rich scale in 60H_2O compared to a mostly Al-rich external layer in 10H_2O after 1,500 h (Figures 6 and 7).

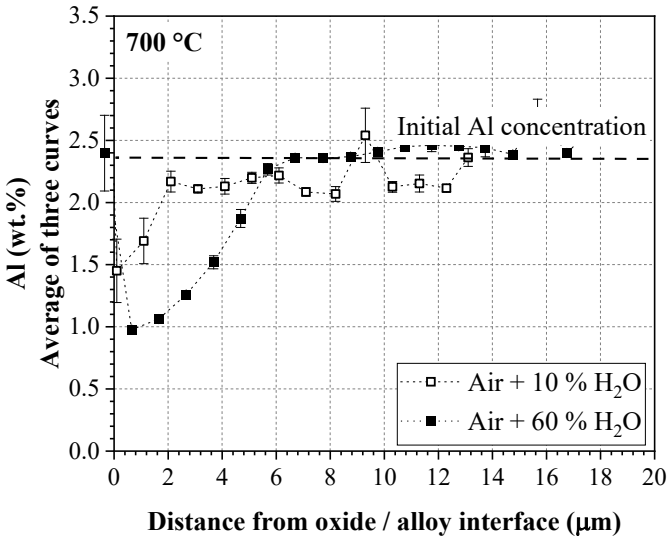

FIGURE 10: EDS AL ELEMENTAL DEPLETION PROFILES WITHIN 602CA (65 µm FOIL THICKNESS) ALLOY AFTER 1,500 H EXPOSURE IN AIR + 10 % H_2O AND AIR + 60 % H_2O AT 700 °C.

The BSE image in Figure 11b of the thicker 602CA alloy foil (200 µm) after 5,000 h in air + 60 % H_2O illustrates the impact of foil thickness on oxidation behavior. For this alloy, the oxide scale was mostly Al-rich (Figure 11b) and some Fe- and Cr-rich oxide nodules were locally formed (Figure 11b) while for the thinner alloy mostly Fe- and Cr-rich external oxides were formed along with Al-rich internal oxides (Figure 11a).

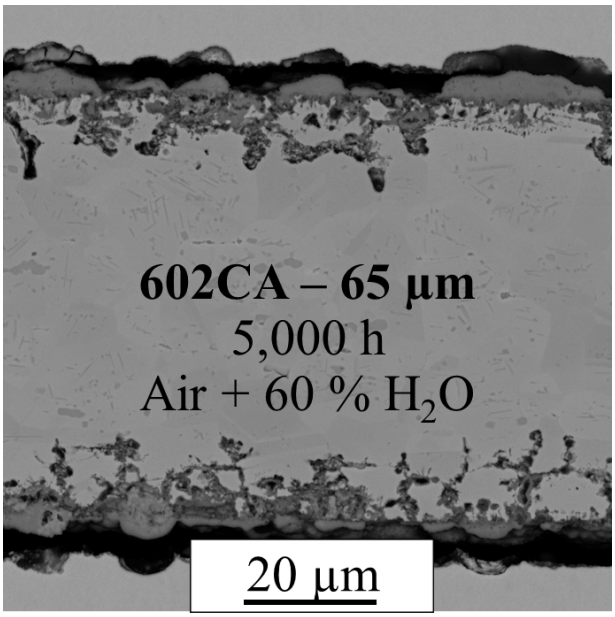

(a)

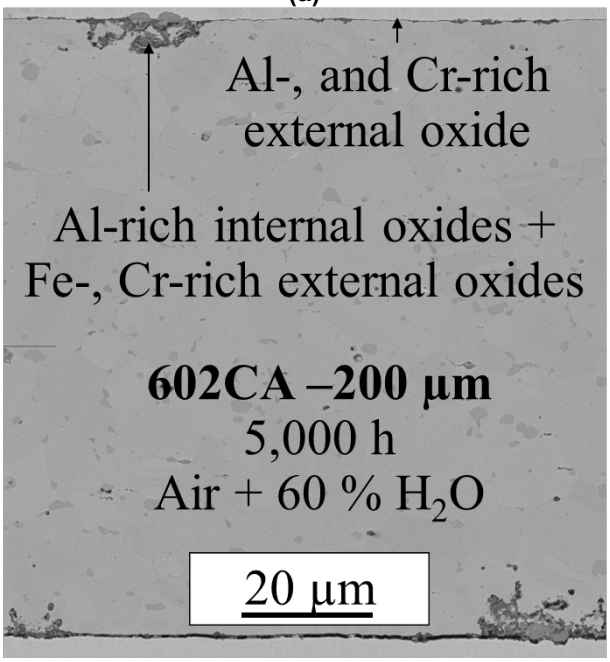

(b)

FIGURE 11: BSE IMAGES OF 602CA ALLOYS (a) 65 µm (b) 200 µm FOIL THICKNESSES AFTER 5,000 H EXPOSURE IN AIR + 60 % H_2O AT 700 °C.

By integrating the EDS Cr and Al depletion profiles at each exposure time, the Cr and Al losses were estimated considering an alloy density of 7.93 $g.cm^{-3}$ (Figure 12). In agreement with the formation of thick Cr-rich oxides in Figure 10, larger Cr and Al losses were measured for the thin 65 µm foil than for the 200 µm specimen after 5,000 h in 60H_2O at 700 °C (Figure 12). These results suggest a faster consumption of oxidizing elements (Al and Cr) for thinner than thicker foils, because of a lower initial (Al or Cr reservoir), and therefore lower oxidation lifetime in service.

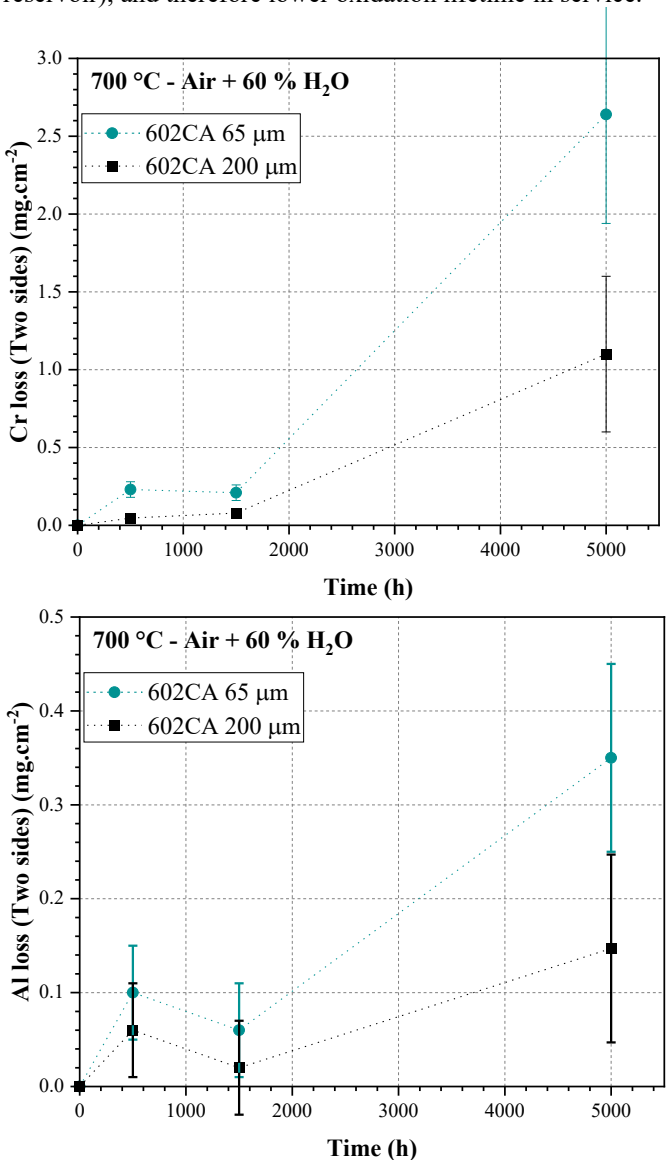

FIGURE 12: EXPERIMENTAL (a) CR AND (b) Al LOSSES AS A FUNCTION OF TIME FOR 602CA 65 AND 200 µm THICK AFTER EXPOSURE IN AIR + 60 % H_2O AND AIR + 60 % H_2O AT 700 °C.

3.3 Oxidation behavior of AFA

In contrast to the 282 and 602CA alloys, a very thin (0.8 ± 0.1 µm) and slow growing Al-rich external oxide and Al-rich acicular internal nitrides were observed for the AFA alloys after 5,000 h in 60H_2O (Figure 13). More detailed nanoscale characterization is needed to precisely define the chemical composition of the observed external scale. Beneath the Al-rich oxide, a precipitate-free zone was observed and corresponded to the oxidation-induced dissolution of the strengthening precipitates (22).

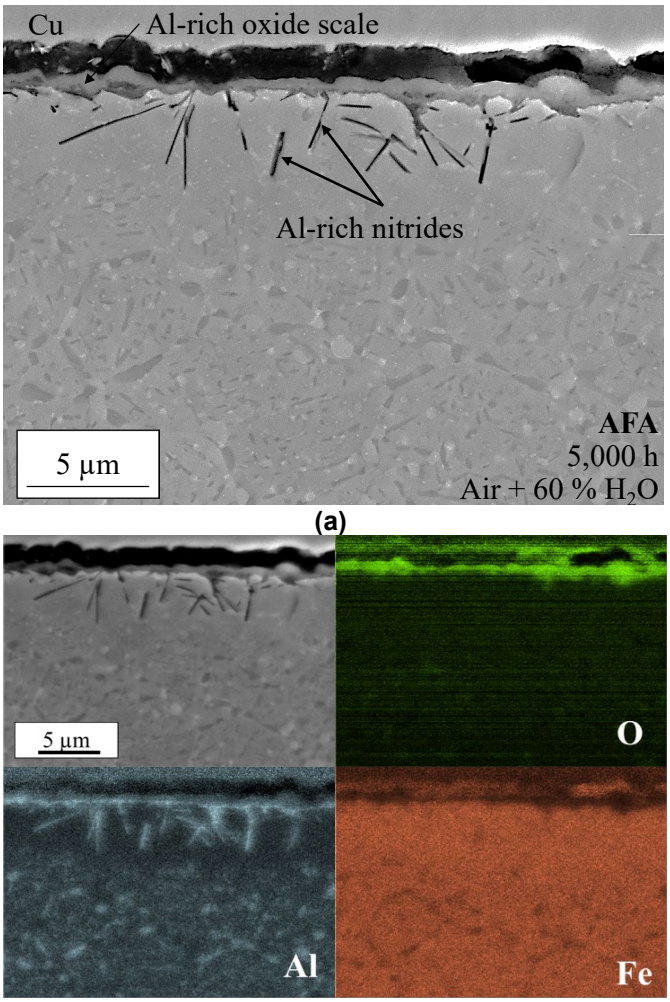

FIGURE 13: (a) BSE IMAGES (b) EDS ELEMENTAL MAPS OF ALLOY AFA AFTER 5,000 H EXPOSURE IN AIR + 60 % H_2O AT 700 °C.

4. DISCUSSION

4.1 Impact of water vapor

The obtained results demonstrated a clear impact of increased water vapor content on the oxidation behavior of 282 specimens. Increased water vapor content in air from 10 to 60 % resulted in greater Cr and Ti losses (Figure 4 and Table 2) and earlier formation of Co- and Ni-rich mixed oxides for 282 (Figure 2). The former observation agrees with the measured lower Cr and Ti interfacial concentrations and slightly deeper depletion depths measured in 282 alloy coupons after 500 h (100 h cycle) exposure in a 60H_2O as compared to 10H_2O (7). The consumption of Cr from the volatilization of Cr_2O_3 into $CrO_2(OH)_2$ (9, 23) (Equation 1) is expected to increase with increasing water vapor content based on the classical gas transport theory since the volatilization rates are directly proportional to the partial pressure of water vapor (10) (Equations 2 and 3).

$$\tfrac{1}{2}\,Cr_2O_3(s) + H_2O\,(g) + \tfrac{3}{4}\,O_2(g) = CrO_2(OH)_2\,(g) \quad (1)$$

$$J_{Cr} = 0.664\,\frac{(p^{(i)}-p^{(0)})}{RT}\left(\frac{D^4}{\nu}\right)^{\frac{1}{6}}\left(\frac{u}{l}\right)^{1/2} M_{\mathrm{Cr}} \quad (2)$$

$$\log\left(p_{\mathrm{CrO_2(OH)_2}}\right) = \log\left(K_{\mathrm{CrO_2(OH)_2}}\right) + \log\left(p_{\mathrm{H_2O}}\right) + 3/4\log\left(p_{\mathrm{O_2}}\right) \quad (3)$$

Pillai and Pint (7) attributed the observed higher depletion of Cr in 282 after 500h at 800 °C in 60H_2O versus 10H_2O to increased Cr_2O_3 volatilization in the higher water vapor containing atmosphere. It has been experimentally shown by Romedenne *et al.* (13, 14) that the combined oxidation and evaporation of the Cr_2O_3 into $CrO_2(OH)_2$ led to higher Cr losses and to the earlier breakdown of the Cr_2O_3 oxide layer in 10H_2O than in dry air for foils (~100 µm) of the Ni-based alloys 625 and 120 between 650 and 800 °C. The formation of Fe-rich oxides was observed on alloy 120 and mixed Nb- and Cr-rich oxides on 625 once the Cr_2O_3 scale formation could not be sustained. In other work by Romedenne *et al.* (15), a more rapid formation of mixed Ti-rich oxides was observed in 10H_2O between 800 and 950 °C compared to dry air. In accordance with theory, a similar finding was observed for 282 with a higher incorporation of Ti in the external oxide scale after 1500 h in 60H_2O than in 10H_2O.

To further elucidate the impact of increased water vapor content in the exhaust atmosphere on oxidation behavior, the model described in (13) was used in the present study to calculate the Cr loss from both oxidation and volatilization. Parabolic oxidation rate constants (k_p) of 1.5×10^{-5} and 1.1×10^{-5} $mg^2.cm^{-4}.h^{-1}$ were used for alloys 282 and 602CA respectively. The k_p values were extrapolated from dry air oxidation data previously reported for 282 and 602CA coupons respectively (Figure 14) (24-26).

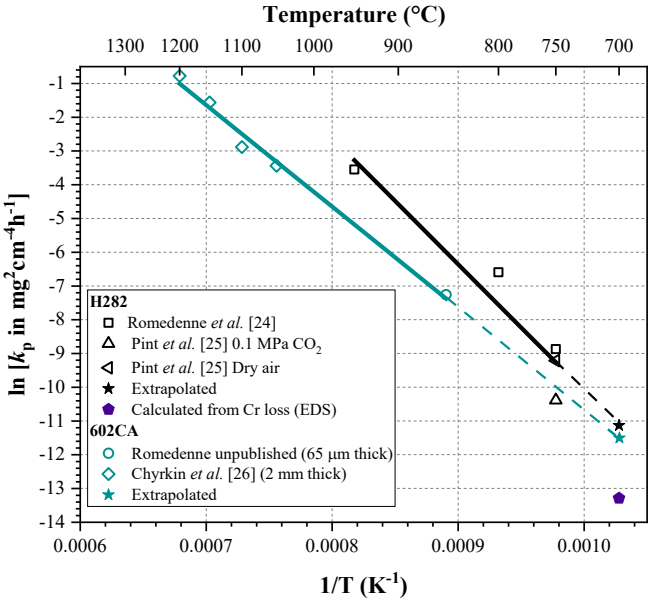

FIGURE 14: OXIDATION RATE CONSTANT OF 282 (BLACK AND 602CA (BLUE) EXTRAPOLATED AT 700 °C FROM VARIOUS LITERATURE SOURCES (24-26).

Then, the volatilization rates (J_{Cr} in mg.cm^{-2}h^{-1}) of chromium were determined using the method described in (10, 13) (Equation 2) with $p^{(i)}$ the partial pressure of $CrO_2(OH)_2$ ($p_{CrO_2(OH)_2}$) from Equation 3, $p^{(0)}$ assumed equal to zero, $K_{CrO_2(OH)_2}$ the $CrO_2(OH)_2$ equilibrium constant value by Gindorf *et al.* (23), p_{H_2O} and p_{O_2} the water and oxygen partial pressures, D as the binary gas diffusion coefficient, R the universal gas constant, T the temperature, v the kinematic viscosity, u the gas velocity, l the specimen length and M_{Cr} the molar mass of Cr.

According to Equations 2 and 3, the Cr loss is linearly proportional to the partial pressure of H_2O (10). The calculated Cr loss in $10H_2O$ and $60H_2O$ compared with experimental measurements are reported in Figure 15. Calculations of total Cr losses can be used to provide information on the overall metal loss of the studied foil. For example, a Cr loss of 1 mg.cm^{-2} after 5,000 h corresponds to a total foil metal loss of 1.2 µm using alloy 282 density of 8.27 g.cm^{-3}.

In agreement with Equation 2 and experimental observations, Figure 15 shows increased calculated Cr loss in $60H_2O$ compared to $10H_2O$. However, the predictions overestimated the Cr loss in $10H_2O$ environment up to 3,500 h (solid lines in Figure 15a). This discrepancy can be attributed to a couple of factors. The extrapolation of k_p, to a value of 1.5×10^{-5} mg^2.cm^{-4}.h^{-1} from mass change literature data at higher temperatures in dry air for 282, is most likely resulting in an overestimation of the real k_p value for the exclusive growth of a Cr_2O_3 scale. Indeed, 282 is known to form a Cr_2O_3 scale with inclusions of Ti-rich oxides and Al- and Ti-rich internal oxides (15, 25), even after a short duration of 500 h at 800 °C. Estimation of rate constants from mass change data will result in apparent (and higher than real) values which include growth of both Cr_2O_3, Ti-rich external oxides and Al-rich internal oxides. Hence, to solely consider the Cr_2O_3 formation, k_p was estimated from the measured Cr depletion profiles (Cr loss) for 282 at 700 °C allowing the calculation of the dash lines in Figure 15a. In this case, the k_p was about 35 % lower (7.5×10^{-6} mg^2.cm^{-4}.h^{-1} in Figure 14) than the value extrapolated from literature data in dry air in Figure 14 (1.5×10^{-5} mg^2.cm^{-4}.h^{-1}). However, this is still an overestimation since it includes Cr loss both due to growth and volatilization. A further reduction in the parabolic rate constant will reduce the discrepancy between experimental and calculated values in $10H_2O$ for 282 (Figure 15a).

Furthermore, the $CrO_2(OH)_2$ equilibrium constant was taken from data by Gindorf *et al.* (23) but large variations have been reported in the literature (9) and could additionally contribute to the discrepancy between the experimental and predicted values. The differences between the measured and predicted Cr losses were significantly less in $60H_2O$ environment for 282 (Figure 15a). This continues to support the earlier discussion because a faster transition to mixed oxides occurred in $60H_2O$ and the employed values for the parabolic rate constants were more representative of the oxidation behavior of 282.

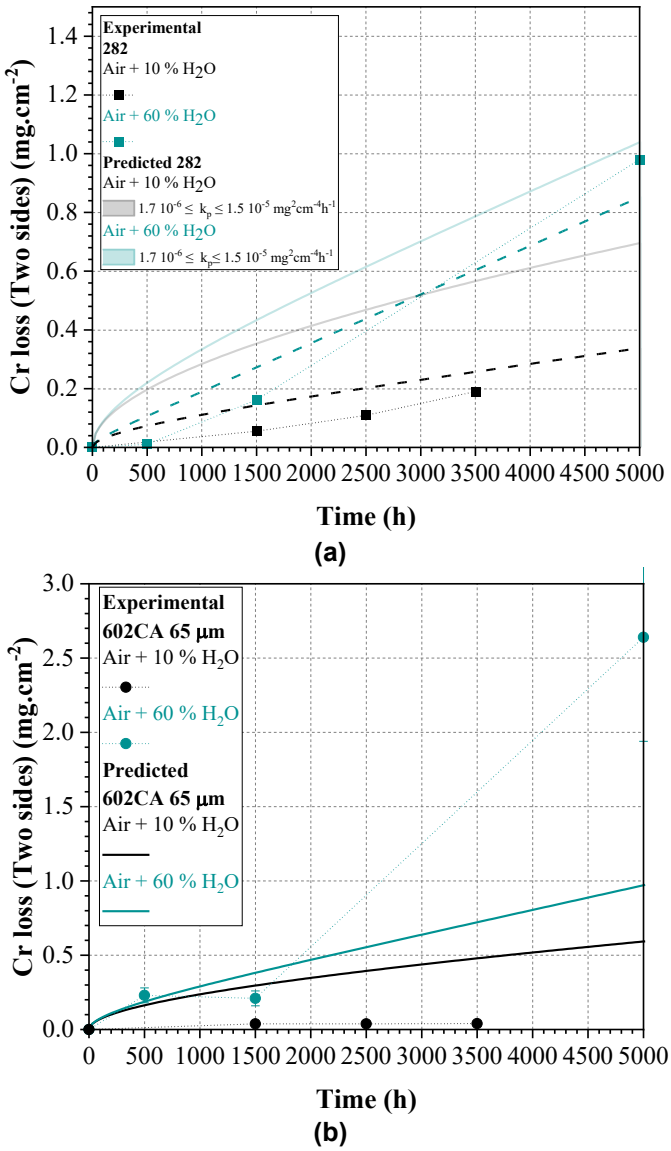

FIGURE 15: EXPERIMENTAL AND CALCULATED CR LOSSES AS A FUNCTION OF TIME FOR (a) 282 AND (b) 602CA 65µm AFTER EXPOSURE IN AIR + 10 % H_2O AND AIR + 60 % H_2O AT 700 °C.

In case of 602CA, the model notably overestimated the Cr losses for 602CA in $10H_2O$ (Figure 15b). As was shown in Figure 6, an external alumina scale was primarily observed to form on 602CA in $10H_2O$ which clearly significantly reduced the Cr losses and could explain the overestimation of Cr losses with the model. In the lifetime model, only Cr_2O_3 formation and volatilization was considered. However, in $60H_2O$, good agreement was obtained between the experimental and predicted Cr losses for the first 1,500 h (Figure 15b) where mostly Cr-rich oxide scale was formed on the surface of the alloy 602CA (Figure 7b). This suggests combined oxidation and volatilization of the Cr-rich scale in $60H_2O$ in agreement with the mass transfer theory presented

above (Equations 1 to 3) for the first 1,500 h. However, after 5,000 h, the model predicted Cr losses about three times lower (1 gm.cm^{-2}) than experimentally measured (2.7 mg.cm^{-2}). The current model accounts for Cr_2O_3 oxidation and volatilization but does not consider the breakdown of the Cr_2O_3 scale into thicker mixed oxides which results in increased Cr and Fe losses. In a previous work, the transition from Cr_2O_3 to thicker mixed oxides was added to the description of the oxidation and volatilization model in the case of 120 and 625 alloy foils during exposure in 10H_2O at 700 and 800 °C. Similarly to this study, the transition to thick mixed oxides resulted in increased Cr loss rates (13) and increased metal loss rates (14). Further work will evaluate the applicability of this improved model to this study and the impact of oxidation- and volatilization-induced microstructural changes (dissolution of strengthening precipitates) (11, 27, 28). Indeed, along with oxidation- and volatilization-induced Cr losses (metal losses), the oxidation-induced evolution of high temperature creep properties during exposure in 60H_2O also needs to be evaluated to select suitable candidate materials for future hydrogen fueled microturbines.

4.2 Impact of composition and foil thickness on oxidation behavior in air + 60 % H_2O

While increased water vapor content in the atmosphere had a detrimental effect on the oxidation behavior and lifetime of the 282 and 602CA alloys, it had little to no effect on the alumina forming AFA alloys after 5,000 h at 700 °C in 60H_2O (Figure 13). These results agree with previous laboratory and engine exposures, where no significant impact of water vapor was observed on the lifetime of AFA foil specimens between 650 and 850 °C in 10H_2O up to 10,000 h (laboratory) and after even longer exposures in engine tests at temperatures estimated below 650°C (29-31). The impact of increased water vapor on the kinetics of formation of α-alumina and its susceptibility to spallation, as reported in the literature for lower water vapor contents (32), remains to be evaluated.

Since the 602CA alloy is a marginal alumina former (33), its ability to form alumina is affected by various factors such as surface finish (34), environments (34) and temperature (26). In the present study, alumina scale was observed mostly in 10H_2O for both thick and thin foils. However, in 60H_2O alumina scale was maintained on the thick 602CA alloy specimens (200 µm) for 5,000 h in 60H_2O at 700 °C (Figure 11). Decreasing the alloy thickness to 65 µm resulted in partial replacement of the alumina scale by external Cr-rich layer and internal Al-rich oxides as a result of lower Cr and Al reservoir than in the thick 602CA specimen (Figures 9 and 11a). During exposure in 60H_2O, as demonstrated earlier, increased volatilization of the Cr-rich external layer led to increased mass losses, Cr losses and to the more rapid transition to thick Fe- and Cr-rich oxides and Al-rich internal oxides (Figure 11a). The present study emphasizes the importance of selecting the right foil thickness for the required lifetime of hydrogen-fueled microturbine foils in service.

5. SUMMARY AND CONCLUSION

High-temperature exposures conducted in air + 10 % H_2O and air + 60% H_2O demonstrated the detrimental effect of increased water vapor content on the long-term oxidation behavior of two chromia-forming Ni-based alloys (282 and 602CA). With the help of an oxidation and volatilization lifetime model, enhanced Cr_2O_3 volatilization was measured and predicted in the higher water vapor-containing atmosphere than in the lower one. The enhanced Cr loss led to the faster transition to thick mixed oxides formation in the case of alloys 282 and 602CA. The oxidation lifetime of the alumina former AFA alloys was not affected by the increased water vapor in the atmosphere during 5,000 h at 700 °C making it a promising candidate for future hydrogen-fueled microturbines. In addition to oxidation and volatilization, loss of high temperature creep properties and impact of foil thickness need to be evaluated for identification of suitable alloy foils of future hydrogen-fueled microturbines.

6. ACKNOWLEDGEMENTS

The authors sincerely thank J. Wade, M. Stephens, T. Lowe and D. Newberry for assistance with the experimental work and metallography preparations and characterization at ORNL. V. Deodeshmukh, S. Dryepondt and H. Hattendorf are acknowledged for providing the 282, AFA and 602CA foils respectively. The authors sincerely thank M. Ridley and D. Sulejmanovic for providing valuable comments on the manuscript. This research was sponsored by the US Department of Energy, Office of Energy Efficiency and Renewable Energy, Combined Heat and Power Program. Notice: This manuscript has been authored by UT-Battelle, LLC under Contract No. DE-AC05-00OR22725 with the U.S. Department of Energy. The United States Government retains and the publisher, by accepting the article for publication, acknowledges that the United States Government retains a non-exclusive, paid-up, irrevocable, world-wide license to publish or reproduce the published form of this manuscript, or allow others to do so, for United States Government purposes. The Department of Energy will provide public access to these results of federally sponsored research in accordance with the DOE PUBLIC ACCESS PLAN (HTTP://ENERGY.GOV/DOWNLOADS/DOE-PUBLIC-ACCESS-PLAN).

REFERENCES

1. Abe JO, Popoola API, Ajenifuja E, Popoola OM. Hydrogen energy, economy and storage: Review and recommendation. International Journal of Hydrogen Energy. 2019;44(29):15072-86.
2. Myers D, Ahluwalia R, Allendorf M, Atwater H, Autrey T, Ayers K, et al. Roundtable on Foundational Science for Carbon-Neutral Hydrogen Technologies (Technology Status Document). Office of Scientific and Technical Information (OSTI); 2021.

3. Hydrogen power with Siemens gas turbines white paper. [Available from: https://www.siemens-energy.com/global/en/news/magazine/2019/hydrogen-capable-gas-turbine.html.
4. The Future of Hydrogen. Paris: International Energy Agency; 2019.
5. Abdalla AM, Hossain S, Nisfindy OB, Azad AT, Dawood M, Azad AK. Hydrogen production, storage, transportation and key challenges with applications: A review. Energ Convers Manage. 2018;165:602-27.
6. Stefan E, Talic B, Larring Y, Gruber A, Peters TA. Materials challenges in hydrogen-fuelled gas turbines. International Materials Reviews. 2021;67(5):1-26.
7. Pillai R, Pint BA. The Role of Oxidation Resistance in High Temperature Alloy Selection for a Future with Green Hydrogen. JOM. 2021;73(12):3988-97.
8. Alvin MA. Materials and Component Development for Advanced Turbine Systems. Proceedings of ASME Turbo Expo 2009, Vol 4. 2009:737-46.
9. Opila EJ, Myers DL, Jacobson NS, Nielsen IMB, Johnson DF, Olminsky JK, et al. Theoretical and experimental investigation of the thermochemistry of $CrO_2(OH)_2(g)$. Journal of Physical Chemistry A. 2007;111(10):1971-80.
10. Young DJ, Pint BA. Chromium volatilization rates from Cr2O3 scales into flowing gases containing water vapor. Oxidation of Metals. 2006;66(3-4):137-53.
11. Pillai R, Dryepondt S, Pint BA. High Temperature Oxidation Lifetime Modeling of Thin-Walled Components. Proceedings of the ASME Turbo Expo: Turbomachinery Technical Conference and Exposition, 2019, Vol 6. 2019.
12. Asteman H, Svensson JE, Johansson LG, Norell M. Indication of chromium oxide hydroxide evaporation during oxidation of 304L at 873 K in the presence of 10% water vapor. Oxidation of Metals. 1999;52(1-2):95-111.
13. Romedenne M, Pillai R, Dryepondt S, Pint BA. Effect of Water Vapor on Lifetime of 625 and 120 Foils During Oxidation Between 650 and 800 °C. Oxidation of Metals. 2021;96(5):589-612.
14. Romedenne M, Pillai R, Dryepondt S, Pint B. Oxidation Lifetime Modeling of 625 and 120 Foils After Long-term Exposure in Flowing Air + 10% H_2O at 700 and 800 °C. Oxidation of Metals. 2022;98(3):305-24.
15. Romedenne M, Haynes A, Pillai R. Cyclic oxidation behavior of selected commercial NiCr-alloys for engine exhaust valves in wet air environment between 800 and 950 °C. Corrosion Sci. 2023;211:110817.
16. Zurek J, Young DJ, Essuman E, Hansel M, Penkalla HJ, Niewolak L, et al. Growth and adherence of chromia based surface scales on Ni-base alloys in high- and low-pO(2) gases. Materials Science and Engineering A. 2008;477(1-2):259-70.
17. Duan R, Jalowicka A, Unocic K, Pint BA, Huczkowski P, Chyrkin A, et al. Predicting Oxidation-Limited Lifetime of Thin-Walled Components of NiCrW Alloy 230. Oxidation of Metals. 2017;87(1):11-38.
18. Croll JE, Wallwork GR. The design of iron-chromium-nickel alloys for use at high temperatures. Oxidation of Metals. 1969;1(1):55-71.
19. Kruger KL. 15 - HAYNES 282 alloy. In: Di Gianfrancesco A, editor. Materials for Ultra-Supercritical and Advanced Ultra-Supercritical Power Plants: Woodhead Publishing; 2017. p. 511-45.
20. Brill U. Neue warmfeste und korrosionsbeständige Nickel-Basis-Legierung für Temperaturen bis 1200°C. Metall. 1992;46(8):778-82.
21. Maziasz P, Swindeman R. Selecting and Developing Advanced Alloys for Creep-Resistance for Microturbine Recuperator Applications. Journal of Engineering for Gas Turbines and Power-transactions of The ASME. 2003;125.
22. Yamamoto Y, Ren Q-Q, Brady M. Role of Cr Content in Microstructure, Creep, and Oxidation Resistance of Alumina-Forming Austenitic Alloys at 850–900 °C. Metals-Basel. 2022;12:717.
23. Gindorf C, Singheiser L, Hilpert K. Vaporisation of chromia in humid air. Journal of Physics and Chemistry of Solids. 2005;66(2-4):384-7.
24. M. Romedenne PS, R. Pillai, S. Dryepondt Isothermal and cyclic oxidation of Haynes 282 processed by Electron Beam Melting
(EBM) and Laser Powder Bed Fusion (LPBF) in dry air at 800 and 950 °C. JOM. 2022;74:1-12.
25. Pint BA, Pillai R, Lance MJ, Keiser JR. Effect of Pressure and Thermal Cycling on Long-Term Oxidation in CO_2 and Supercritical CO_2. Oxidation of Metals. 2020;94(5-6):505-26.
26. Chyrkin A, Sloof WG, Pillai R, Galiullin T, Grüner D, Quadakkers WJ. Modelling compositional changes in nickel base-alloy 602 CA during high temperature oxidation. Materials at High Temperatures. 2015;32(1-2):102-12.
27. Chyrkin A, Pillai R, Ackermann H, Hattendorf H, Richter S, Nowak W, et al. Modeling carbide dissolution in alloy 602 CA during high temperature oxidation. Corrosion Sci. 2015;96:32-41.
28. Pillai R, Chyrkin A, Galiullin T, Wessel E, Gruener D, Quadakkers WJ. External alpha-Al2O3 scale on Ni-base alloy 602 CA - Part II: Microstructural evolution. Corrosion Sci. 2017;127:27-38.
29. Pint BA, Dryepondt S, Brady MP, Yamamoto Y, Ruan B, McKeirnan RD. Field and Laboratory Evaluations of Commercial and Next-Generation Alumina-Forming Austenitic Foil for Advanced Recuperators. Journal of Engineering for Gas Turbines and Power-Transactions of the Asme. 2016;138(12).
30. Dryepondt S, Pint BA. Validation of Lifetime Models for Recuperator Foils Through Long-Term Laboratory and Engine Testing. Volume 8: Microturbines, Turbochargers, and Small Turbomachines; Steam Turbines2019.
31. Romedenne M, Pillai R, Dryepondt S, Lance M, Pint B. High Temperature Oxidation Behavior of Fe- and Ni-Based Alloy Foils in Water Vapor at 850 °C. NACE CORROSION2021.

32. Saunders SRJ, Monteiro M, Rizzo F. The oxidation behaviour of metals and alloys at high temperatures in atmospheres containing water vapour: A review. Progress in Materials Science. 2008;53(5):775-837.
33. Young DJ. High temperature oxidation and corrosion of metals. 1st ed. Oxford: Elsevier; 2008. 535 p.
34. Schiek M, Niewolak L, Nowak W, Meier GH, Vassen R, Quadakkers WJ. Scale Formation of Alloy 602 CA During Isothermal Oxidation at 800-1100 degrees C in Different Types of Water Vapor Containing Atmospheres. Oxidation of Metals. 2015;84(5-6):661-94.